Proceedings of the ASME/BATH 2023
Symposium on Fluid Power and Motion Control
FPMC2023
October 16-18, 2023, Sarasota, FL, USA

FPMC2023-111868

PRACTICAL IMPLEMENTATION OF SECONDARY CONTROL PRINCIPLES IN AN ELECTRO-HYDRAULIC SPEED-VARIABLE DRIVE APPLIED TO AN INJECTION MOULDING MACHINE

Rasmus A. Hertz[1,*], Ole Therkelsen[1], Søren Kristiansen[2], Jesper K. Christensen[3], Christian-Emil Helver[4], Lasse Schmidt [4]

[1]R&D Moulding, LEGO System A/S
[2]Materials Department, LEGO System A/S
[3]Moulding Analytics Center, LEGO System A/S
[4]AAU Energy, Aalborg University

ABSTRACT

In this work, a hydraulic state of the art injection molding machine is retrofitted with a dual pump drive. The dual pump drive is an electro-hydraulic speed-variable drive, with focus on high bandwidth control through secondary control principles. Secondary control is based on providing the torque references for the electric machines directly, instead of a speed reference. The pressure control loop is based on decoupling of the piston load pressure and sum pressure enabling the possibility to utilize two SISO controllers. The application is the injection cylinder of an industrial injection molding machine, retrofitted with the designed dual pump drive. Experimental results for the proposed secondary control structure are presented and difficulties of implementation are documented, and a large gap between the theoretical achievable bandwidth and the experimental achievable bandwidth is shown. Three possible reasons for this gap are identified, namely amplification of high frequency components from e.g. signal noise on sensors, the use of axial piston pumps which induce pressure pulsations and the influence of the discrete sample time of the digital controller hardware. Lastly future work within the field is considered, including possible methods to minimize the influence of the identified issues.

Keywords: Electro-Hydraulic Variable-Speed Drive, Secondary Control

1. INTRODUCTION

The effectiveness of a feedback system to minimise the influence of disturbances from e.g. external forces is related to the bandwidth of the system and the control design. Previous research in the field of electro-hydraulic speed-variable drives, have focused on two control strategies namely primary control and secondary control. Primary control is based on utilizing the speed control loop in the electric motor and drive, whereas secondary control utilizes the torque loop in the controller. The bandwidth of the torque loop is, in general, a decade higher than the bandwidth of the velocity and position loop of the motor drive, theoretically allowing pressure control at a higher bandwidth [1]. The main difference between the two control strategies is that, in the velocity-controlled servo drive, the speed of the motor is proportional to the flow out of the displacement unit with a pressure reaction. This is the traditional method to control hydraulic machines also when considering e.g. valve control. For the torque controlled servo drive, the torque is correlated with the force on the piston, meaning the torque is correlated to the chamber pressures through a flow coupling [1].

There exist multiple configurations of electro-hydraulic speed-variable drives, and an overview of the different topologies can be found in [2]. Primary research are based on a single motor connected to two displacement units described in [1, 3–7] etc. and two motors and two displacement units adding an additional degree of freedom described in [8–11] etc., all mainly applying primary control approaches. This paper focuses on the development of secondary control for a dual pump drive (DPD) including two pumps and motors, retrofitted on an industrial state of the art (SOA) injection moulding machine, controlling the hydraulic injection cylinder. According to [12], injection moulding requires both velocity and force control, as well as smooth switchover between the two. However, this paper exclusively concentrates on force control, given the similarity in challenges for both aspects. A force and level pressure controller is derived and implemented on a digital controller, with experimental results from the machine showcasing the difficulty in realising the theory on a physical setup. The differences between the model and the physical setup, including the digital control implementation, are outlined and the limitations are discussed.

Previous research within secondary control of hydraulic systems utilising electro-hydraulic speed-variable drives are limited to [1, 13] solely focus on the theoretical aspects and have not yet undergone any practical implementation or testing on an actual setup. The retrofit of the electro-hydraulic speed-variable drive

*Corresponding author: Rasmus.Aagaard.Hertz@LEGO.com

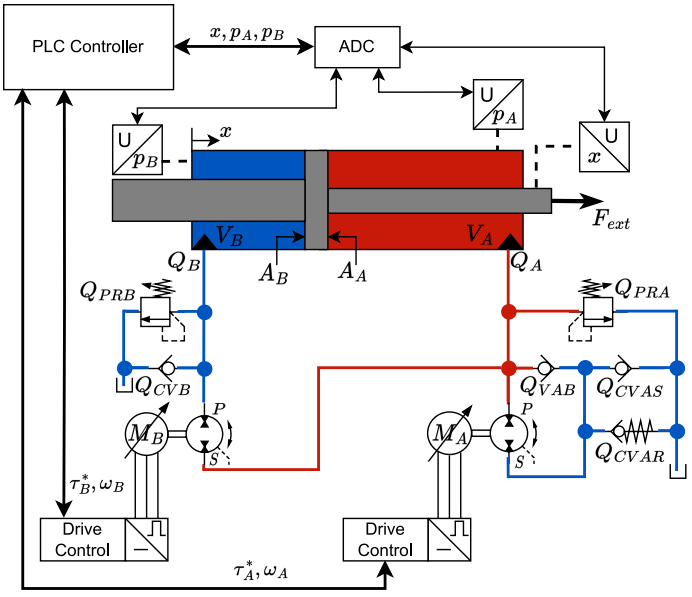

FIGURE 1: ELECTRIC AND HYDRAULIC OVERVIEW OF THE DPD.

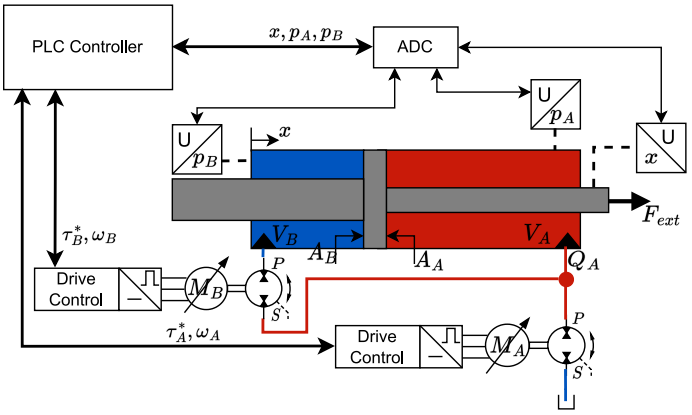

FIGURE 2: SIMPLIFIED ELECTRIC AND HYDRAULIC OVERVIEW OF THE DPD.

are designed according to Fig. 1. The focus in the design phase has been to remove valves from the primary flow paths. The valves in the flow path is limited to check valves and pressure relief valves, that ensures anti-cavitation and safety respectively. Valves are not used in general operation, which means that a reduced diagram containing only relevant hydraulic components for general operation is shown in Fig. 2. The controller design is based on a lumped parameter model, which is designed from a physically motivated approach, according to the methodology described in [1, 14], as contrary to complex algorithms like [15–19].

2. SYSTEM MODEL

The lumped parameter model is based on the schematic shown in Fig. 2. The pressure dynamics for the two chambers are given in Eqs. (1) - (2).

$$\dot{p}_A = \frac{\beta_A}{V_{A,I} + A_A(L-x)}(Q_A - Q_B - C_{Lc}(p_A - p_B) + A_A\dot{x}),$$
$$Q_A = D_A\omega_{mA} - k_A Q_{LPA}, \quad Q_B = D_B\omega_{mB} - k_B Q_{LPB} \quad (1)$$

$$\dot{p}_B = \frac{\beta_B}{V_{B,I} + A_B x}(Q_B + C_{Lc}(p_A - p_B) - A_B\dot{x}) \quad (2)$$

Where β_A and β_B is the bulk modulus, $V_{A,I} = 1.4 \cdot 10^{-3}$ m^3 and $V_{B,I} = 1.6 \cdot 10^{-3}$ m^3 is the initial chamber volumes, $A_A = 7.8 \cdot 10^{-3}$ m^2 and $A_B = 2.7 \cdot 10^{-3}$ m^2 is the effective area of each side of the piston, $C_{Lc} = 5 \cdot 10^{-16}$ m^3/Pa is the leakage coefficient across the cylinder piston and $D_A = 16$ ccm/rev and $D_B = 8.1$ ccm/rev is the pump displacements. The pump leakage $Q_{LPA} = Q_{LPA}(p_A, p_T, \omega_A)$ and $Q_{LPB} = Q_{LPB}(p_A, p_B, \omega_B)$ are estimated from [20]. The pump leakage are scaled based on the displacement fraction through the two constants $k_A = 0.592$ and $k_B = 0.296$, similar to [21].

The states are the chamber pressures p_A and p_B, the motor velocities ω_A and ω_B, the piston velocity $\dot{x}$ and the position of the piston x. Bulk modulus of the oil is approximated by Eq. 3.

$$\beta_n = \left(\frac{1}{\beta_{oil}} + \left(\frac{\epsilon_{air,0} p_{atm}}{n_{oil} p_n^2}\right)\right)^{-1} \quad (3)$$

Where $n_{oil} = 1.4$ is the polytropic exponent, $\beta_{oil} = 9.5 \cdot 10^8$ Pa is the maximum value of bulk modulus of the oil, p_n is the pressure of chamber $n = [A, B]$, $\epsilon_{air,0} = 0.005$ % is the air percentage in the oil at atmospheric pressure and $p_{atm} = 1 \cdot 10^5$ Pa is the atmospheric pressure.

The movement of the cylinder is deducted based on Newton's second law of motion shown in Eq. (4)

$$\ddot{x} = \frac{1}{m}(-p_A A_A + p_B A_B - F_C sgn(\dot{x}) - B_v\dot{x} + F_{ext}) \quad (4)$$

Where $m = 250$ kg is the mass of the piston and injection unit, $F_C = 1241$ N is the columb friction, $B_v = 6480\frac{\text{N·s}}{\text{m}}$ is the viscous friction and the sgn function is the sigmoid function to ensure a continues solution. As the motors are in torque control mode, the torque balance of motor and pump is stated in Eqs. (5) - (6).

$$\dot{\omega}_A = \frac{1}{J_A}\left(\tau_A - \tau_{Afric} - D_A(p_A - p_T)\right),$$
$$\tau_{Afric} = \tau_{CA}\text{sgn}(\omega_A) + B_{vA}\omega_A \quad (5)$$

$$\dot{\omega}_B = \frac{1}{J_A}\left(\tau_B - \tau_{Bfric} - D_B(p_B - p_A)\right),$$
$$\tau_{Bfric} = \tau_{CB}\text{sgn}(\omega_B) + B_{vB}\omega_B \quad (6)$$

Where $J_A = 9.3 \cdot 10^{-3}$ kg·m^3 and $J_B = 8.7 \cdot 10^{-3}$ kg·m^3 is the rotational inertia of motor and pump for respectively motor A and motor B. τ_{Afric} and τ_{Bfric} is the friction of the motor and pump, consisting of a coulomb friction term $\tau_{CA} = 4.5$ Nm and $\tau_{CB} = 2.8$ Nm and a viscous friction term $B_{vA} = 0.04$ N·s/rad and $B_{vA} = 0.01$ N·s/rad. The last term in the two equations represent the external force from the hydraulic system on the motor, represented as the the loading on the pumps. The torque controller located inside the motor drive is approximated by a first

order system. In general for electric machines a approximation of the bandwidth is a decade below the switching frequency ω_{SC}. The motor torque dynamics is given in Eq. (7).

$$\dot{\tau_n} = \frac{\omega_{SW}}{10}(\tau_n^* - \tau_n) \tag{7}$$

Where τ_n^* and τ_n is the reference torque and the actual torque of the motor $n = [A, B]$. $\omega_{SW} = 4$ kHz is the switching frequency of the inverter.

2.1 State Space Representation

The state space representation is the foundation for linear analysis of the system, used to understand the input output couplings in the system. The system is linearized through first order Taylor expansion at an equilibrium point. The leakage across the cylinder, the Coulomb friction terms, the tank pressure and the external force are considered disturbances. As the pressure is kept at a minimum pressure bulk modulus is assumed constant. The linearised pump flows are given by Eqs. (8) and (9).

$$Q_A = D_A\omega_A - k_A(C_{L\omega A}\omega_A + C_{LpA}p_A) \tag{8}$$
$$Q_B = D_B\omega_B - k_B(C_{L\omega B}\omega_B + C_{LpB}(p_B - p_A)) \tag{9}$$

The Taylor expansion for the chamber pressure gradients are shown in Eqs. (10) - (11).

$$\begin{aligned}\Delta\dot{p}_{AL} =& \left.\frac{\partial\dot{p}_A}{\partial x}\right|_{\mathbf{x}_0}\Delta x + \left.\frac{\partial\dot{p}_A}{\partial\dot{x}}\right|_{\mathbf{x}_0}\Delta\dot{x} + \left.\frac{\partial\dot{p}_A}{\partial p_A}\right|_{\mathbf{x}_0}\Delta p_A + \left.\frac{\partial\dot{p}_A}{\partial p_B}\right|_{\mathbf{x}_0}\Delta p_B + \\ & \left.\frac{\partial\dot{p}_A}{\partial\omega_A}\right|_{\mathbf{x}_0}\Delta\omega_A + \left.\frac{\partial\dot{p}_A}{\partial\omega_B}\right|_{\mathbf{x}_0}\Delta\omega_B \end{aligned} \tag{10}$$

$$\begin{aligned}\Delta\dot{p}_{BL} =& \left.\frac{\partial\dot{p}_B}{\partial x}\right|_{\mathbf{x}_0}\Delta x + \left.\frac{\partial\dot{p}_B}{\partial\dot{x}}\right|_{\mathbf{x}_0}\Delta\dot{x} + \left.\frac{\partial\dot{p}_B}{\partial p_A}\right|_{\mathbf{x}_0}\Delta p_A + \left.\frac{\partial\dot{p}_B}{\partial p_B}\right|_{\mathbf{x}_0}\Delta p_B + \\ & \left.\frac{\partial\dot{p}_B}{\partial\omega_A}\right|_{\mathbf{x}_0}\Delta\omega_A + \left.\frac{\partial\dot{p}_B}{\partial\omega_B}\right|_{\mathbf{x}_0}\Delta\omega_B \end{aligned} \tag{11}$$

Where $\mathbf{x}_0 = [x_0\ \dot{x}_0\ p_{A0}\ p_{BO}\ \omega_{A0}\ \omega_{B0}]^T$ is the equilibrium point. The analysis furthermore focus on force control in end stop ($x = 0$). Lastly a minimum pressure is kept in the low pressure side meaning $p_{B0} = p_{set}$. Utilising these assumptions the equilibrium point can be calculated from $\dot{p}_A = 0$ and $\dot{p}_B = 0$ as Eq. (12).

$$\begin{aligned} x_0 &= 0 \\ \dot{x}_0 &= 0 \\ p_{A0} &= \frac{F_{ext} + p_{B0}A_B}{A_A} \\ p_{BO} &= p_{set} \\ \omega_{A0} &= -\frac{1}{k_A c_{L\omega A} - D_A}\big(p_{A0}(k_A c_{LpA} + k_b c_{LpB}) - c_{LpB}k_B p_{B0} \\ &\quad + \omega_{B0}(-k_B c_{L\omega B} + D_B)\big) \\ \omega_{B0} &= \frac{k_B c_{LpB}(p_{A0} - p_{B0})}{c_{L\omega B}k_B - dB} \end{aligned} \tag{12}$$

Where $p_{set} = 30 \cdot 10^5$ Pa and $F_{ext} = 27000$ N. The linearized chamber volumes are given in Eqs. (13) - (14).

$$V_{A0} = V_{A,I} + A_A(L - x_0) \tag{13}$$
$$V_{B0} = V_{B,I} + A_B x_0 \tag{14}$$

The design of the pressure controller will be based on a cascaded control structure, assuming that the bandwidth of the torque control loop is 5-10 faster than the pressure control loop. This makes it possible to simplify the system matrix by disregarding the inverter and motor dynamics and assume $\tau_n = \tau_n^*$. It is now possible to generate the the state space system from Eqs. (4) - (6) and (8) - (14) disregarding the terms that are considered disturbances. The state space system is shown in Eq. (15).

$$\dot{\mathbf{x}} = \mathbf{A}\mathbf{x} + \mathbf{B}\mathbf{u}, \quad \mathbf{y} = \mathbf{C}\mathbf{x}, \quad \mathbf{x} = \begin{bmatrix} x & \dot{x} & p_A & p_B & \omega_A & \omega_B \end{bmatrix}^T$$
$$\mathbf{u} = \begin{bmatrix} \tau_A^* & \tau_B^* \end{bmatrix}^T, \quad \mathbf{A} =$$
$$\begin{bmatrix} 0 & 1 & 0 & 0 & 0 & 0 \\ 0 & -\frac{B_v}{m} & -\frac{A_A}{m} & \frac{A_B}{m} & 0 & 0 \\ 0 & \frac{\beta A_A}{V_{A0}} & -\frac{\beta k_{pA}}{V_{A0}} & \frac{\beta k_{pB}}{V_{A0}} & \frac{\beta k_{\omega A}}{V_{A0}} & -\frac{\beta k_{\omega B}}{V_{A0}} \\ 0 & -\frac{\beta A_B}{V_{B0}} & \frac{\beta k_{pB}}{V_{B0}} & -\frac{\beta k_{pB}}{V_{B0}} & 0 & \frac{\beta k_{\omega B}}{V_{B0}} \\ 0 & 0 & -\frac{D_A}{J_A} & 0 & -\frac{B_{VA}}{J_A} & 0 \\ 0 & 0 & \frac{D_B}{J_B} & -\frac{D_B}{J_B} & 0 & -\frac{B_{VB}}{J_B} \end{bmatrix},$$
$$k_{pA} = k_A C_{LpA} + k_B C_{LpB}, \quad k_{\omega A} = D_A - k_A C_{L\omega A}$$
$$k_{pB} = k_B C_{LpB}, \quad k_{\omega B} = D_B - k_B C_{L\omega B}$$
$$\mathbf{B} \begin{bmatrix} 0 & 0 \\ 0 & 0 \\ 0 & 0 \\ 0 & 0 \\ \frac{1}{J_A} & 0 \\ 0 & \frac{1}{J_B} \end{bmatrix}, \quad \mathbf{C} \begin{bmatrix} 0 & 0 & 1 & 0 & 0 & 0 \\ 0 & 0 & 0 & 1 & 0 & 0 \end{bmatrix} \tag{15}$$

The linearised constants are $\beta_0 = 9.5 \cdot 10^8$ Pa, $V_{A0} = 2.5 \cdot 10^{-3}$ m^3, $V_{B0} = 1.6 \cdot 10^{-3}$ m^3, $C_{LpA} = 2.73 \cdot 10^{-13}$ m^3/(Pa·s), $C_{LpB} = 1.36 \cdot 10^{-13}$ m^3/(Pa·s), $C_{L\omega A} = 2.69 \cdot 10^{-8}$ m^3 and $C_{L\omega B} = 1.34 \cdot 10^{-8}$m^3. The input output couplings are analysed using RGA elements. The transfer function matrix is given by Eq. (16).

$$\mathbf{G} = \mathbf{C}(s\mathbf{I} - \mathbf{A})^{-1}\mathbf{B} \tag{16}$$

The RGA plot shown in Fig. 3 of the input pairing $p_A(\tau_A^*)$, $p_B(\tau_B^*)$ and $p_A(\tau_B^*)$,$p_B(\tau_A^*)$ shows that the RGA elements are changing implying that significant input output-couplings are present. An injection moulding machine should be capable of running with multiple moulds and materials, meaning the external force is unknown and can change rapidly depending on mould geometry [22]. This requires the load pressure on the cylinder to be tightly coupled to an input of the system independent of frequency.

3. STATE DECOUPLING

It is desired to decouple the system due to the required robustness of the process. An input and output decoupling is proposed translating the input torques and output pressure measurements

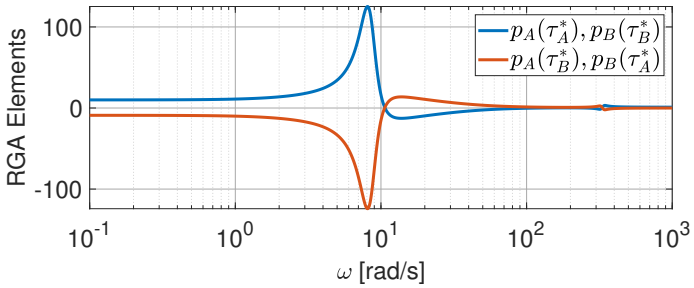

FIGURE 3: RGA ELEMENTS OF THE ORIGINAL SYSTEM, SHOWING THAT THE BEST INPUT OUTPUT PAIRING CHANGES IN THE FREQUENCY RANGE.

into virtual states. These virtual states makes it possible to control the load pressure and sum pressure independently. The output and input transformation are described independently.

3.1 Output Decoupling

The two pressure states are rewritten to virtual pressure states, one related to the cylinder force (p_L) and one related the pressure level (p_H) in the chambers. The virtual output pressures are defined in Eq. (17).

$$p_L = p_A - \alpha p_B, \quad p_H = p_A + p_B, \quad \alpha = \frac{A_B}{A_A} \tag{17}$$

3.2 Input Decoupling

The input decoupling should determine the input torque τ_A^* and τ_B^* to the two motors to control the two virtual output states p_L and p_H. As the torque is introduced through the motors angular acceleration, the desired dynamics can be described as a second order system through Eqs. (18) and (19)

$$\ddot{p_L} = \omega_L^2(p_L^* - p_L) - 2\zeta_L\omega_L\dot{p_L} \tag{18}$$
$$\ddot{p_H} = \omega_H^2(p_H^* - p_H) - 2\zeta_H\omega_H\dot{p_H} \tag{19}$$

From the second order system it is possible to choose the desired eigenfrequency and damping through the parameter ζ_n and ω_n respectively for $n = [L, H]$. Here a cascaded controller structure is utilised in this case, meaning ω_n should be chosen in the region of 5-10 times slower than the torque control loop in the inverter and motor setup given in Eq. (7). The theoretical possible bandwidth of the torque controlled setup is therefore 40 Hz. This can be substantially raised if the switching frequency of the inverter is increased to 8 or 16 kHz. However increasing the switching frequency will introduce additional switching losses.

The first and second derivative of the load pressure and sum pressure given in Eq. (17) is given in Eqs. (20) and (21).

$$\dot{p}_L = \dot{p}_A - \alpha\dot{p}_B, \quad \ddot{p}_L = \ddot{p}_A - \alpha\ddot{p}_B \tag{20}$$
$$\dot{p}_H = \dot{p}_A + \dot{p}_B, \quad \ddot{p}_H = \ddot{p}_A + \ddot{p}_B \tag{21}$$

The second derivative of the chamber pressures are calculated from Eqs. (1) and (2). The equation is further simplified by assuming a slow varying bulk modulus ($\beta_n(t) \approx \beta_n$), which is reasonable as the low pressure chamber is kept at a minimum pressure. It is further assumed that the volume change is slow varying ($V_n(t) \approx V_n$). As the leakage terms are based on look-up tables and non-differentiable the linearized pump flows from Eqs. (8) and (9) are substituted into the chamber pressure dynamics for the controller design.

The derivative of the chamber pressure dynamics is given in Eqs. (22) and (23).

$$\ddot{p}_A = \frac{\beta_A}{V_A}(\dot{Q}_A - \dot{Q}_B - C_{Lc}(\dot{p}_A - \dot{p}_B) + A_A\ddot{x}), \tag{22}$$
$$\dot{Q}_A = D_A\dot{\omega}_A - k_A C_{L\omega A}\dot{\omega}_A - k_A C_{LpA}\dot{p}_A$$
$$\dot{Q}_B = D_B\dot{\omega}_B - k_B C_{L\omega B}\dot{\omega}_B - k_B C_{LpB}(\dot{p}_A - \dot{p}_B)$$
$$\ddot{p}_B = \frac{\beta_B}{V_B}(\dot{Q}_B + C_{Lc}(\dot{p}_A - \dot{p}_B) - A_B\ddot{x}) \tag{23}$$

From Eqs. (1), (2), (5),(6), (20) -(23) it is possible to solve for the two motor torque τ_{mA} and τ_{mB}. The full equation is omitted due to space limitation; however, if the bandwidth and damping are chosen, it is possible to rewrite the torque references to be a function of the variables $x, \dot{x}, \ddot{x}, p_L^*, p_H^*, \omega_A, \omega_B$ shown in Eqs. (24)- (25).

$$\tau_A^* = f(\beta_A, \beta_B, x, \dot{x}, \ddot{x}, p_L^*, p_L, p_H^*, p_H, \omega_A, \omega_B) \tag{24}$$
$$\tau_B^* = f(\beta_A, \beta_B, x, \dot{x}, \ddot{x}, p_L^*, p_L, p_H^*, p_H, \omega_A, \omega_B) \tag{25}$$

A reference for the motor torque has successfully been established, generated from system constants, bandwidth, damping, and states. A limitation to the proposed controller is that it requires measurement of bulk modulus, velocity, and acceleration which are impractical to measure. However as previously assumed, if the bulk modulus is varying slowly and the pressure in both chambers are minimum p_{set} it can be approximated by a constant. With respect to the velocity and acceleration it is depending on the piston movement, for force control with low speeds and acceleration they are approximately zero. For motion-controlled cases the velocity and acceleration can be approximated from the trajectory. The rewritten torque reference is stated in Eqs. (26)-(27).

$$\tau_A^* = f(x, \hat{\dot{x}}, \hat{\ddot{x}}, p_L^*, p_L, p_H^*, p_H, \omega_A, \omega_B) \tag{26}$$
$$\tau_B^* = f(x, \hat{\dot{x}}, \hat{\ddot{x}}, p_L^*, p_L, p_H^*, p_H, \omega_A, \omega_B) \tag{27}$$

Where $\hat{\dot{x}}$ and $\hat{\ddot{x}}$ is the estimated velocity and acceleration respectively, from the motion controller at speeds different from zero.

3.3 Coupling analysis

It is desired to reformulate the input and output decoupling into a linearized system to investigate the couplings across a desired frequency range. As discussed above, the desired piston velocity and acceleration trajectory is needed in the decoupling if $\dot{x} \neq 0$. A constrained simplified case, representing load holding situations which is also present in injection moulding is studied to ensure the decoupling is successful. The piston is placed in $x = 0$, and the system can be modeled as interlocked as $\ddot{x} = \dot{x} = 0$. This reduces the states to Eq. (28).

$$\mathbf{x}_s = \begin{bmatrix} p_A & p_B & \omega_A & \omega_B \end{bmatrix}^T \tag{28}$$

The input output decoupling is presented for the special case of $\ddot{x} = \dot{x} = 0$ by introducing the output decoupling matrix W_O

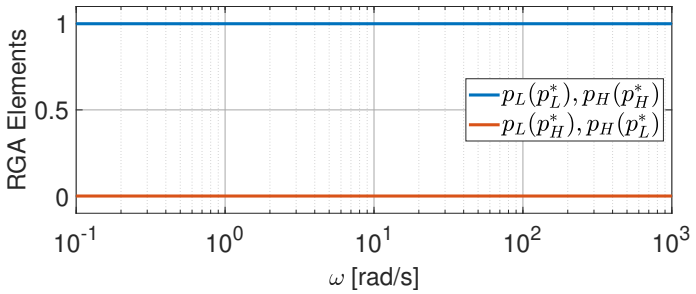

FIGURE 4: RGA ELEMENTS OF THE AUGMENTED SYSTEM, THAT SHOWS THE SYSTEM IS DECOUPLED.

and the input decoupling matrix related to the states in W_{Is} and the input decoupling in matrix W_{Ir}. The decoupling matrices for a state space representation of the system is stated in Eqs. (29) -(31).

$$W_O = \begin{bmatrix} 1 & -\alpha & 0 & 0 \\ 1 & 1 & 0 & 0 \\ 0 & 0 & 1 & 0 \\ 0 & 0 & 0 & 1 \end{bmatrix} \tag{29}$$

$$W_{Ir} = \begin{bmatrix} \frac{\partial \tau_A^*}{\partial p_L^*} & \frac{\partial \tau_A^*}{\partial p_H^*} \\ \frac{\partial \tau_B^*}{\partial p_L^*} & \frac{\partial \tau_B^*}{\partial p_H^*} \end{bmatrix} \tag{30}$$

$$W_{Is} = \begin{bmatrix} \frac{\partial \tau_A^*}{\partial p_L} & \frac{\partial \tau_A^*}{\partial p_H} & \frac{\partial \tau_A^*}{\partial \omega_A} & \frac{\partial \tau_A^*}{\partial \omega_B} \\ \frac{\partial \tau_B^*}{\partial p_L} & \frac{\partial \tau_B^*}{\partial p_H} & \frac{\partial \tau_B^*}{\partial \omega_A} & \frac{\partial \tau_B^*}{\partial \omega_B} \end{bmatrix} \tag{31}$$

W_{Ir} and W_{Is} is only denoted by the partial derivatives due to the size of the matrix. From the input output decoupling matrices a decoupled state space system is presented in Eq. (32) derived based on augmented system matrices in Eq. (33)

$$\begin{aligned} &\dot{\mathbf{x}}_s = \hat{\mathbf{A}}\mathbf{x}_s + \hat{\mathbf{B}}\hat{\mathbf{u}}, \quad \hat{\mathbf{y}} = \hat{\mathbf{C}}\mathbf{x}_s, \quad \mathbf{x}_s = \begin{bmatrix} p_A & p_B & \omega_A & \omega_B \end{bmatrix}^T \\ &\hat{\mathbf{u}} = \begin{bmatrix} p_L^* & p_H^* \end{bmatrix}^T, \quad \hat{\mathbf{y}} = \begin{bmatrix} p_L & p_H & \omega_A & \omega_B \end{bmatrix}^T \end{aligned} \tag{32}$$

$$\begin{aligned} &\hat{\mathbf{A}} = \mathbf{A}_{[3:6,3:6]} + \mathbf{B}_{[3:6,:]}\mathbf{W}_{Is}\mathbf{W}_O, \quad \hat{\mathbf{B}} = \mathbf{B}_{[3:6,:]}\mathbf{W}_{Ir}, \\ &\hat{\mathbf{C}} = \mathbf{C}_{[3:6,3,6]}\mathbf{W}_O \end{aligned} \tag{33}$$

From the augmented system matrices the RGA elements are plotted again to ensure the system is decoupled and it is possible to control p_L by p_L^* and p_H by p_H^*. Figure 4 shows that the system is fully decoupled as expected, which means that it is possible to control the load and the sum pressure as desired.

4. SUM PRESSURE REFERENCE

The sum pressure reference should be designed to ensure a minimum pressure p_{set} in the low pressure chamber of the cylinder. The low pressure side can be determined based on comparison of the chamber pressures. The sum pressure reference is given in Eq. (34)

$$\begin{aligned} &\text{if} \quad p_A \geq p_B, \quad p_{set} = p_B: \quad p_H^* = p_A + p_{set} \\ &\text{if} \quad p_A < p_B, \quad p_{set} = p_A: \quad p_H^* = p_{set} + p_B \end{aligned} \tag{34}$$

Remark the load pressure reference is continues at all times. It would now be possible to design a motion controller to control both position and velocity in a cascaded controller structure with the pressure controller as the inner loop. Motion control is also an important part of the injection moulding process. It further requires a reference switchover, swithching from the velocity to pressure control [12], however as the scope of this paper is high bandwidth pressure control this has been omitted.

5. EXPERIMENTAL RESULTS

The designed controller is implemented on the retrofitted industrial injection moulding machine, according to the schematic in Fig. 1. The digital controller communicates with the motor drives and sensors over etherCAT® with a cycle time of 2 ms. The wires for the analog sensors are kept as short as possible with a maximum length of 0.4 m, to minimise the amount og noise on the chamber pressure signals. The two motors are permanent magnet synchronous motors connected to a drive, with internal torque control. The focus on the hydraulic side have been to keep volumes as small as possible in e.g. hoses, as this will increase the possible pressure gradients as less flow of oil is needed to elevate the pressure. The pumps utilised are fixed displacement piston pumps, with 9 pistons in each pump.

To test the designed load and sum pressure controller utilising secondary control a load pressure reference is designed. The load pressure reference is designed as a series of random steps with the constraint that $p_L > 0$ shown in Fig. 5a. To ensure that the piston velocity is equal to zero when testing the load pressure controller, it is moved to $x = 0$. As described in Section 3.2 the theoretical obtainable bandwidth is approximately 40 Hz, however, after implementation, a tuning of the controller was needed due to an unstable inner torque loop. The tuned physically realisable bandwidth on the proposed setup is 16 Hz. The controller gains are $\omega_L = 100$ rad/s, $\omega_H = 80$ rad/s and a damping of $\zeta = 1$ to avoid oscillations. As $\omega_H < \omega_L$ the bandwidth of the load pressure controller is larger than the bandwidth of the sum pressure controller. This ensures that the load pressure control is prioritized. The bulk modulus estimate is $\beta = 9.5 \cdot 10^8$ Pa, which is assumed valid due to the elevated low pressure side. Velocity and acceleration reference are both equal zero as there is no movement of the piston. Figure 5b shows the load pressure tracking capability in both the experimental setup and the simulation. Both experiment and simulation show that a steady state error is present contributed to the fact that the controller does not contain an integrator and simplifications in the controller design from e.g. pump leakage approximation. The load pressure error is shown in Fig. 5c, where it is seen that the steady-state error in the simulation is smaller than in the experiment. Increasing the bandwidth of ω_L and ω_H minimises the steady state error, due to an increased gain. The chamber pressures p_A and p_B are shown in Figs. 5d-5e where it can be seen that the low-pressure chamber changes depending on the desired load pressure due to the difference in piston area in the two chambers. In addition, it is seen that the low pressure side is kept at a minimum $p_{set} = 30 \cdot 10^5$ Pa.

From the plots of pressure in Fig. 5b-5e it can be seen that the experimental data shows large oscillations each time a step

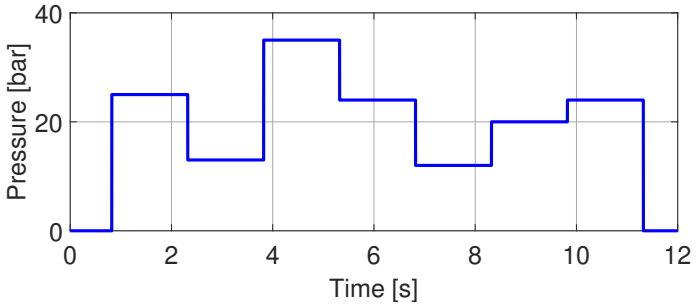

(a) Reference to the load pressure controller p_L^*.

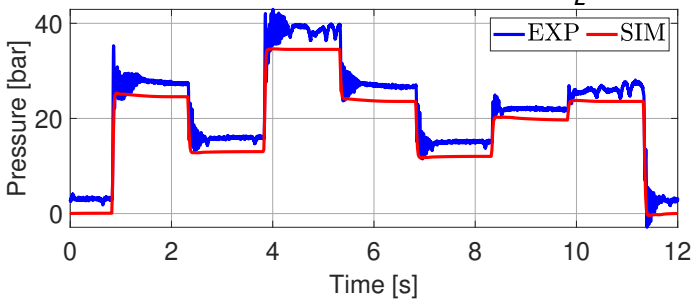

(b) Load pressure p_L.

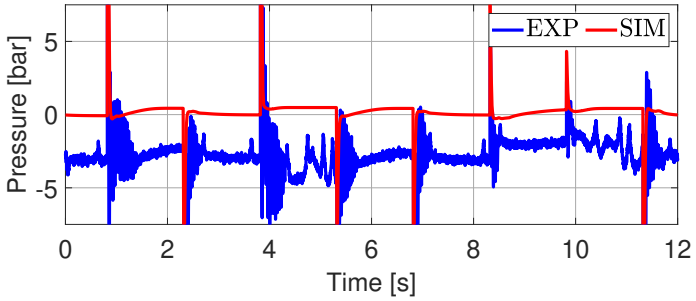

(c) Load pressure error ($p_L^* - p_L$), spikes at the time of step is outside plot.

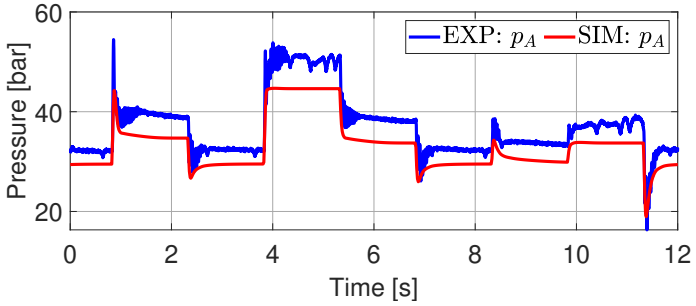

(d) Chamber pressure p_A.

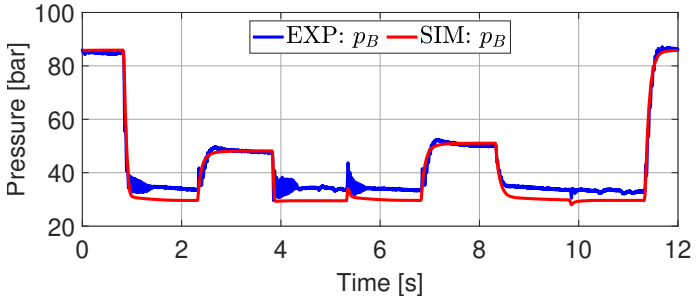

(e) Chamber pressure p_B.

FIGURE 5: LOAD AND SUM PRESSURE CONTROLLER PERFORMANCE.

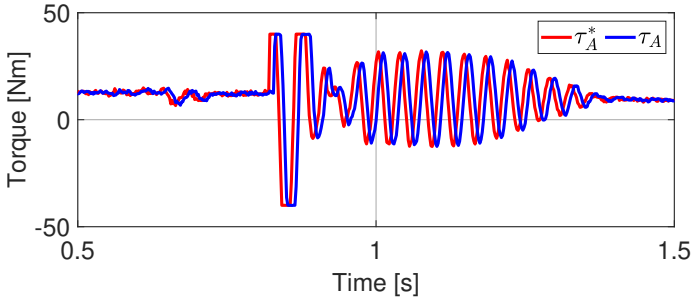

(a) Torque motor A.

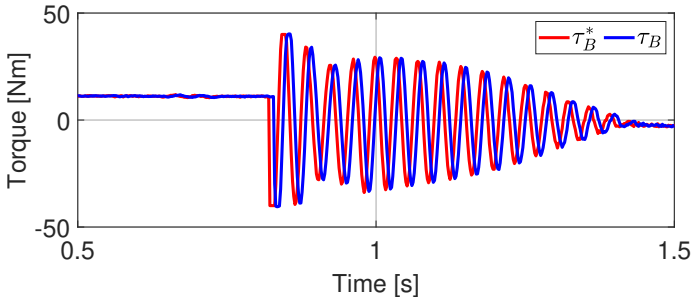

(b) Torque motor B.

FIGURE 6: TORQUE REFERENCE AND ACTUAL TORQUE FOR THE TWO MOTORS.

in reference occur. These oscillations changes dependent on the controller gains. A plot of the torque reference for a smaller time sequence are sown in Fig. 6 where it is confirmed that the motor torque in the experiment have oscillations whereas the simulation model does not and is therefor not plotted. It can further be seen that the torque at the step input is reaching the saturation shortly. This is mainly due to the oscillations and it raises the question; Why is such a large gap present between the theoretical estimated bandwidth of 40 Hz and the achieved bandwidth of 16 Hz?

6. DISCUSSION

To consider the possible reasons for not obtaining the desired bandwidth, there might be several reasons both independently and in combination. In this work three reasons have been identified and are being considered in the following. These are related to sensor noise, pressure drops from the pumps and the delay introduced in the digital controller and communication architecture.

6.1 Signal Noise

Signal noise is inevitable in experimental setups, but can be minimised through mindful installation shielding and grounding. A main difference between the model and the experiment is the amount of noise in the pressure signal. Figure 7 shows a selection of a pressure signal, where the pressure is elevated following a stop of both motors meaning $\omega_A = \omega_B = 0$ rad/s at end stop. The data are created without the use of the filter in the analog-to-digital converter. Most analog to digital converters do have built in filters; however, they often have a too low cut-off frequency if considered utilized for secondary control. The magnitude of the noise is approximately ±0.2 bar. The dominating noise frequencies are at approximately 200 Hz, estimated from a fourier

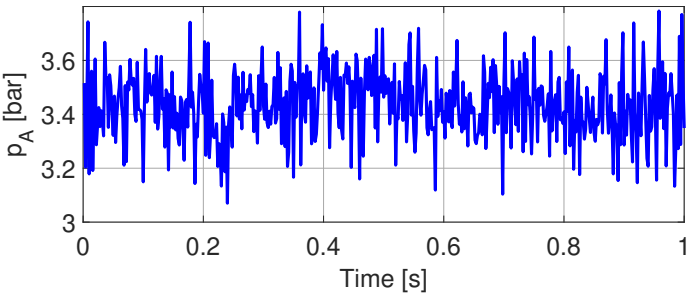

FIGURE 7: PRESSURE (p_A) AT ELEVATED PRESSURE WITH $\omega_A = \omega_B = 0$ RPM.

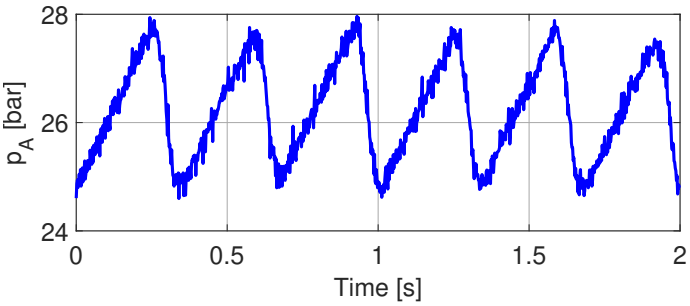

FIGURE 8: PRESSURE (p_A) AT $\omega_A = 10$ RPM.

transform. Much of the noise at 200 Hz should be attenuated according to the frequency response for the system $\omega_L = 40$ Hz. The 200 Hz noise component which approximately is 2000 rad/s are attenuated with -40 dB. This indicates that this is not the only cause of the gap between theoretical and experimental bandwidth.

6.2 Pressure Pulsations

Another source of noise in the system comes from the hydraulic piston pumps. Due to the design with 9 finite pistons, a given number of pressure pulses are expected at the port of each pump. Each piston comes in contact with the inlet and outlet of the pump one time per revolution resulting in a total of 18 contacts per revolution. Ideally the piston is only in contact with one chamber at a time, to ensure a minimum of leakage between inlet and outlet of the pump. However due to the sinusoidal movement of each piston inside the pump is it necessary with a small overlap to avoid cavitation in the oil. This overlap suddenly introduces a leakage path from the high pressure to the low pressure side, creating a rapid decrease in pressure The effect on the pressure in chamber A is investigated by moving the cylinder to the end position, locking motor B while running motor A with 10 RPM. The resulting chamber pressure at steady state is shown in Fig. 8. From the figure it is seen that the pressure drops approximately 3 times per second, resulting in a frequency of 18 pulses per revolution as expected. The noise from the pressure pulses will be within the bandwidth of the closed loop system as they have a frequency of 3 Hz at 10 rpm which is a present velocity in load holding situations. The magnitude of the pulses are also much larger than the electric noise with a magnitude of 2.5 bar at a chamber pressure of 10 bar and a motor angular velocity of 10 rpm. The shape of the drop is almost triangular, indicating the pressure drop occurs suddenly, when high and low pressure side are short circuited to avoid cavitation. The pressure builds up relatively slower afterwards as the piston pushes oil into the high pressure side.

6.3 Time Delay

The controller is designed in a continues time environment where the gain is aplied continuously on the plant. However the digital controller run in discrete time steps, in this case the limit of cycle time is the etherCAT® bus capable of running at 500 Hz. This makes it possible to update the motor torques at each 2 ms, additionally it will be at least another 2 ms to measure the change in pressure. The delay in the system is estimated to 6-8 ms. The communication frequency of 500 Hz introduces a delay combined with a zero-order hold in the system that needs to be accounted for. In high bandwidth applications, a delay could cause instability. The effect of a delay can be analysed in the linear system. In the Laplace domain it is given by Eq. (35).

$$G_D(s) = e^{Ts} \tag{35}$$

Where T is the delay. The zero-order hold of the signal is disregarded, as the effect is assumed to be negligible compared to the time constant of the hydraulic system. The analysis is based on the special case where $\ddot{x} = \dot{x} = 0$, the states are shown in Eq. (28) and the decoupling matrices shown in Eq. (33) are valid. The dynamics of the motor controller shown in Eq. (7) are not considered. The transfer function between p_L^* and p_L is analyzed as $\omega_L > \omega_H$, which corresponds to $\mathbf{G_{sys}}(1,1)$ in Eq. (36).

$$\mathbf{G_{sys}} = (\hat{\mathbf{C}}(s\mathbf{I} - \hat{\mathbf{A}})^{-1}\hat{\mathbf{B}})G_D(s) \tag{36}$$

The influence of delays on the closed loop pole and zero locations are approximated with a Padé approximation. As a cascaded controller structure is proposed, the maximum bandwidth of the pressure loop, which is 40 Hz, is investigated. The system is assumed stable if all closed loop poles are in the left half plane, however this requirement can cause oscillating systems. Figure 9 shows the possible bandwidth as a function of the amount of delay. The blue line represents the marginally stable system, and the colored area below is the stable region. It can be seen that the delay in the digital controlled system has a large effect on the possible obtainable bandwidth. It can further be seen that a maximum delay of 3 ms is required if the bandwidth of 40 Hz should be reached. It is further seen that the approximately 16 Hz tuned in the experiment is close to the theoretical maximum achievable, with the 6-8 ms delay present in the in the test setup.

7. FUTURE WORK

The future work in realisation of high bandwidth hydraulic systems using electro-hydraulic speed-variable actuators and secondary control, should strive to overcome the challenges with noise, pressure pulsations and communication delays in the digital controller. The sensor noise could possibly be minimised adding analog filters where it is possible to select the desired cut off frequency at a frequency above the desired bandwidth of the closed loop pressure controller. Another solution could be to

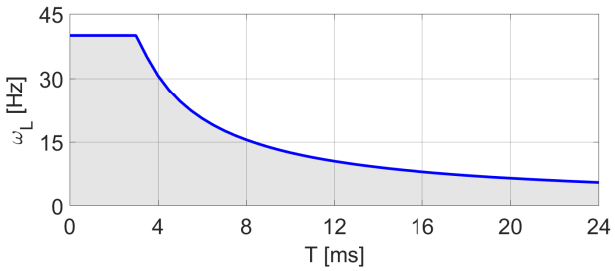

FIGURE 9: STABILITY MAPPING OF $G_{sys}(1,1)$ DEPENDENT ON THE DELAY T AND BANDWIDTH ω_L.

employ "digital" pressure sensors, meaning no analog wiring is needed.

The pressure pulsations occurring due to the finite number of chambers and the leakage pathway between the high and low pressure side, is due to anti cavitation needs in the pumps. The amount of leakage could possibly be minimised by a different design of the anti cavitation system [20]. As the motor design is difficult to change, it is desired to consider it as a control problem. In systems with larger volumes in front of the pump, the lower eigenfrequency will automatically damp the effect. The volume of the pump should also be considered to ensure running as little as possible in low velocity modes where the leakage pathway will be present at longer times. Lastly filtering of the ripples should be considered to ensure the controller does not react on the pressure ripple.

Any delay in any control system is undesired, it has been shown that a delay above 3 ms, will make the closed loop system unstable. This should be considered when choosing the hardware. EtherCAT® communication with faster cycle times are obtainable with other types of hardware, unfortunately this has not been available for this work.

8. SUMMARY

A secondary controlled electro-hydrualic speed-variable drive is proposed to realise high bandwidth control of a retrofitted hydraulic injection moulding machine. According to the theory bandwidths of at least 40 Hz is achievable. However when implemented on the experimental setup the achievable bandwidth proved to be only approximately 16 Hz. Three main contributors to this discrepancy were considered, namely sensor noise, ripples from the hydraulic pumps and delay in the control system. Delay in the system is seen as the main contributor as it theoretically has been shown the system becomes unstable due to this delay. Lastly future endeavours in the field of secondary control of electro-hydraulic speed-variable drives are discussed, to make it possible to realise control bandwidths in vicinity of the theoretically possible.

ACKNOWLEDGMENTS

This work is funded by LEGO System A/S.

REFERENCES

[1] Schmidt, Lasse, Ketelsen, Søren, Grønkær, Nikolaj and Hansen, Kenneth Vorbøl. "On Secondary Control Principles in Pump Controlled Electro-Hydraulic Linear Actuators." *BATH/ASME 2020 Symposium on Fluid Power and Motion Control*. 2020. American Society of Mechanical Engineers Digital Collection. DOI 10.1115/FPMC2020-2722.

[2] Ketelsen, Søren, Padovani, Damiano, Andersen, Torben O., Ebbesen, Morten Kjeld and Schmidt, Lasse. "Classification and Review of Pump-Controlled Differential Cylinder Drives." *Energies* Vol. 12 No. 7 (2019): p. 1293. DOI 10.3390/en12071293.

[3] Agostini, Thales, De Negri, Victor, Minav, Tatiana and Pietola, Matti. "Effect of Energy Recovery on Efficiency in Electro-Hydrostatic Closed System for Differential Actuator." *Actuators* Vol. 9 No. 1 (2020): p. 12. DOI 10.3390/act9010012.

[4] Zhang, Shuzhong, Li, Su and Minav, Tatiana. "Control and Performance Analysis of Variable Speed Pump-Controlled Asymmetric Cylinder Systems under Four-Quadrant Operation." *Actuators* Vol. 9 No. 4 (2020): p. 123. DOI 10.3390/act9040123.

[5] Casoli, Paolo, Scolari, Fabio, Minav, Tatiana and Rundo, Massimo. "Comparative Energy Analysis of a Load Sensing System and a Zonal Hydraulics for a 9-Tonne Excavator." *Actuators* Vol. 9 No. 2 (2020): p. 39. DOI 10.3390/act9020039.

[6] Schmidt, Lasse, Ketelsen, Søren, Padovani, Damiano and Mortensen, Kasper Aa. "Improving the Efficiency and Dynamic Properties of a Flow Control Unit in a Self-Locking Compact Electro-Hydraulic Cylinder Drive." *ASME/BATH 2019 Symposium on Fluid Power and Motion Control*. 2019. American Society of Mechanical Engineers Digital Collection. DOI 10.1115/FPMC2019-1671.

[7] Schmidt, Lasse, Ketelsen, Søren, Brask, Morten Helms and Mortensen, Kasper Aastrup. "A Class of Energy Efficient Self-Contained Electro-Hydraulic Drives with Self-Locking Capability." *Energies* Vol. 12 No. 10 (2019): p. 1866. DOI 10.3390/en12101866.

[8] Helduser, Siegfried. "Electric-Hydrostatic Drive Systems and Their Application in Injection Moulding Machines." *Proceedings of the JFPS International Symposium on Fluid Power* Vol. 1999 No. 4 (1999): pp. 261–266. DOI 10.5739/isfp.1999.261.

[9] Ketelsen, Søren, Andersen, Torben Ole, Ebbesen, Morten Kjeld and Schmidt, Lasse. "Mass Estimation of Self-Contained Linear Electro-Hydraulic Actuators and Evaluation of the Influence on Payload Capacity of a Knuckle Boom Crane." *ASME/BATH 2019 Symposium on Fluid Power and Motion Control*. 2019. American Society of Mechanical Engineers Digital Collection. DOI 10.1115/FPMC2019-1689.

[10] Ketelsen, Søren, Andersen, Torben Ole, Ebbesen, Morten K. and Schmidt, Lasse. "A Self-Contained Cylinder Drive with Indirectly Controlled Hydraulic Lock." Vol. 41 No. 3 (2020): pp. 185–205. DOI 10.4173/mic.2020.3.4.

[11] Ketelsen, Søren, Padovani, Damiano, Kjeld Ebbesen, Morten, Andersen, Torben Ole and Schmidt, Lasse. "A Gasless Reservoir Solution for Electro-Hydraulic Compact

Drives With Two Prime Movers." *BATH/ASME 2020 Symposium on Fluid Power and Motion Control*. 2020. American Society of Mechanical Engineers Digital Collection. DOI 10.1115/FPMC2020-2773.

[12] Hertz, Rasmus A, Christensen, Jesper K, Therkelsen, Ole, Kristiansen, Søren, Helver, Christian-Emil, Hansson, Frederik A and Schmidt, Lasse. "A Novel Approach to Control Switchover Between Injection and Holding Phase for a Hydraulic Injection Moulding Machine." *ANTEC23*. 2023. Denver.

[13] Schmidt, Lasse, Ketelsen, Søren, Mommers, Robin and Achten, Peter. "Analogy Between Hydraulic Transformers and Variable-Speed Pumps." *BATH/ASME 2020 Symposium on Fluid Power and Motion Control*. 2020. American Society of Mechanical Engineers Digital Collection. DOI 10.1115/FPMC2020-2719.

[14] Schmidt, Lasse and Hansen, Kenneth Vorbøl. "Electro-Hydraulic Variable-Speed Drive Networks—Idea, Perspectives, and Energy Saving Potentials." *Energies* Vol. 15 No. 3 (2022): p. 1228. DOI 10.3390/en15031228.

[15] Schmidt, Lasse, Andersen, Torben O., Pedersen, Henrik C. and Bech, Michael M. "2-SMC of Electro-Hydraulic Drives Using the Twisting Algorithm." *Applied Mechanics and Materials* Vol. 233 (2012): pp. 131–134. DOI 10.4028/www.scientific.net/AMM.233.131.

[16] Schmidt, Lasse and Andersen, Torben O. "Application of Second Order Sliding Mode Algorithms for Output Feedback Control in Hydraulic Cylinder Drives with Profound Valve Dynamics." *e & i Elektrotechnik und Informationstechnik* Vol. 133 No. 6 (2016): pp. 238–247. DOI 10.1007/s00502-016-0425-7.

[17] Schmidt, Lasse, Andersen, Torben O. and Pedersen, Henrik C. "On Application of Second Order Sliding Mode Control to Electro-Hydraulic Systems." *ASME 2014 12th Biennial Conference on Engineering Systems Design and Analysis*. 2014. American Society of Mechanical Engineers Digital Collection. DOI 10.1115/ESDA2014-20470.

[18] Schmidt, Lasse, Andersen, Torben O., Johansen, Per and Pedersen, Henrik C. "A Robust Control Concept for Hydraulic Drives Based on Second Order Sliding Mode Disturbance Compensation." *ASME/BATH 2017 Symposium on Fluid Power and Motion Control*. 2017. American Society of Mechanical Engineers Digital Collection. DOI 10.1115/FPMC2017-4265.

[19] Schmidt, Lasse, Andersen, Torben O. and Pedersen, Henrik C. "An Approach for Second Order Control With Finite Time Convergence for Electro-Hydraulic Drives." *ASME/BATH 2013 Symposium on Fluid Power and Motion Control*. 2014. American Society of Mechanical Engineers Digital Collection. DOI 10.1115/FPMC2013-4441.

[20] "Performance of Hydrostatic Machines - Extensive Measurement Report." Technical report no. INNAS BV. 2020.

[21] Padovani, Damiano, Ketelsen, Søren, Hagen, Daniel and Schmidt, Lasse. "A Self-Contained Electro-Hydraulic Cylinder with Passive Load-Holding Capability." *Energies* Vol. 12 No. 2 (2019): p. 292. DOI 10.3390/en12020292.

[22] Hertz, Rasmus Aa, Christensen, J. K., Kristiansen, S., Therkelsen, O. and Schmidt, L. "In-Line Process and Material Property Measurement in Injection Moulding - a Theoretical Review." *Production & Manufacturing Research* Vol. 10 No. 1 (2022): pp. 938–963. DOI 10.1080/21693277.2022.2148136.